J Adv Ceram

Research Article

Strongly polarizable nanodomains enable excellent energy storage performance at moderate electric fields in lead-free $Bi_{0.5}Na_{0.5}TiO_3$-based ceramics

Wanjin Li[1], Pu Mao[1,5,✉], Xinyang Zhao[1], Ting Wang[2], Tianyu Li[3,✉], Yahui Tian[4], Zhiyong Liu[1], Bing Xie[1], Kun Guo[1], Jinghui Gao[5]

Cite this article: Li W, Mao P, Zhao X, et al. *J Adv Ceram* 2026, **15**(5): 9221289. https://doi.org/10.26599/JAC.2026.9221289

ABSTRACT: The simultaneous achievement of high recoverable energy storage density (W_{rec}) and high efficiency (η) under moderate electric fields remains a critical challenge for dielectric ceramic capacitors in modern electronic systems, despite their ultrahigh power density and rapid charge-discharge capabilities. Here, we propose a strategy to construct strongly polarizable nanodomains, enabling excellent energy storage performance (ESP) under moderate electric fields in $Bi_{0.5}Na_{0.5}TiO_3$ (BNT)-based ceramics. Compositional modulation by multiple cations, together with a regulative proportion of rhombohedral (*R*) and tetragonal (*T*) phases, enhances random fields, weakens interdomain interactions, forms strongly polarizable nanodomains, and elevates the breakdown strength (E_b) without sacrificing the intrinsic high polarity of the matrix. Consequently, the optimized $0.98(BNSB)_{0.985}S_{0.01}T$–0.02CMN ceramic exhibits an ultrahigh maximum polarization (P_{max}) of 65.8 μC/cm², with slim polarization–electric (*P*–*E*) field loops. Owing to these features, the optimized bulk ceramic achieves a record W_{rec} of 6.11 J/cm³ and an impressive η of 86% at an E_b of 330 kV/cm. Moreover, this sample also presents outstanding temperature/frequency stability and charging–discharging performance. These findings suggest that the $(BNSB)_{1-1.5y}S_yT$–0.02CMN component has immense potential for advanced pulse power capacitors under a moderate applied electric field and further offers a valid avenue for exploring high-performance lead-free dielectric materials.

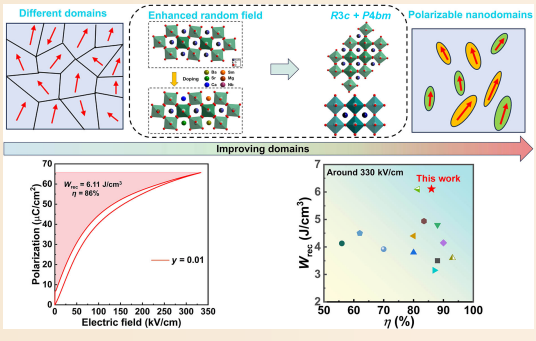

KEYWORDS: $Bi_{0.5}Na_{0.5}TiO_3$-based lead-free ceramics; multiphase design; strongly polarizable nanodomains; energy storage performance; ultrahigh polarization

1 Introduction

With increasing global energy demand and decreasing fossil fuel reserves, efficient energy storage and utilization have become increasingly crucial for sustainable technological advancement [1–3]. Dielectric ceramic capacitors are prized for their rapid charging–discharging capabilities and high-power density, positioning them as key elements in pulsed-power and electronic applications. However, a persistent challenge lies in attaining both high recoverable energystorage density (W_{rec}) and high efficiency (η) concurrently, which is constrained by the fundamental trade-off between polarization and the breakdown strength (E_b), hindering further miniaturization, lightweighting, and integration [4–11]. Generally, the energy storage performance (ESP) of dielectric ceramics is evaluated by Eqs. (1)–(3) [12,13]:

$$W_{total} = \int_0^{P_{max}} E\mathrm{d}P \tag{1}$$

$$W_{rec} = \int_{P_r}^{P_{max}} E\mathrm{d}P \tag{2}$$

$$\eta = \frac{W_{rec}}{W_{total}} \times 100\% \tag{3}$$

where P is the polarization, P_{max} is the maximum polarization, and P_r is the remnant polarization, respectively. The breakdown behavior and polarization response of the dielectric materials jointly determine the W_{rec} and η of the dielectric capacitors.

[1] Jiangxi Key Laboratory of Extreme Manufacturing Technology for High-End Equipment, School of Materials Science and Engineering, Nanchang Hangkong University, Nanchang 330603, China. [2] Guangdong Provincial Key Laboratory of Electronic Functional Materials and Devices, Huizhou University, Huizhou 516001, China. [3] School of Materials Science and Engineering, University of Science and Technology, Beijing 100083, China. [4] School of Information Engineering, Jiangxi University of Technology, Nanchang 330098, China. [5] State Key Laboratory of Electrical Insulation and Power Equipment, Xi'an Jiaotong University, Xi'an 710049, China.

✉ Corresponding authors. E-mail: P. Mao, pumao@nchu.edu.cn; T. Li, tianyuli@ustb.edu.cn

Received: January 8, 2026; Revised: March 6, 2026; Accepted: March 24, 2026

Therefore, dielectric capacitors that combine high P_{max} with large E_b are vital for realizing superior ESPs.

Lead-free relaxor ferroelectric ceramics have attracted considerable attention because of their near-zero P_r and low dielectric loss [14–26]. Among them, $Bi_{0.5}Na_{0.5}TiO_3$ (BNT) stands out as a representative lead-free relaxor ferroelectric possessing high spontaneous polarization ($P_s \approx 38$ μC/cm²) originating from strong Bi $6s^2$–O 2p orbital hybridization [27,28]. Such a feature, however, favors high W_{rec}, yet the large coercive field and high dielectric loss (tanδ) limit their practical use in advanced capacitors [29]. In addition, Bi volatility during high-temperature sintering and the tendency toward coarse grain formation are universal phenomena in BNT-based ceramic systems, which can limit the increase in E_b [30,31]. To address these issues, several strategies, such as local structural design, polar nanodomain engineering, and defect engineering, have been adopted to increase the ESP of BNT-based ceramics [30,32–35]. Nevertheless, these approaches often introduce nonpolarizable networks or end members that, while improving the voltage endurance, inevitably suppress the polarization strength [36]. In addition, capacitors operating under high electric fields suffer from severe thermal accumulation and even thermal breakdown. Hence, it is imperative to develop approaches capable of maintaining strong polarization and high η, particularly under moderate electric fields.

In this work, we propose a strategy to construct strongly polarizable nanodomains within BNT-based ceramics, wherein the regulative proportion of *R* and *T* phases, combined with the enhanced random field via multi-ion substitution, weakens interdomain interactions and increases E_b, forming strongly polarizable nanodomains. Therefore, the intrinsic high polarity of the matrix is effectively preserved. The incorporation of Sm^{3+} ions further amplifies local structural heterogeneity, stabilizing the regulative proportion of *R* and *T* phases and promoting the evolution of polar nanoregions (PNRs) with diverse sizes. These features collectively lead to the formation of strongly polarizable nanodomains. Compared with conventional polar nanodomains, it has a higher inherent polarizability and displays large field-induced polarization and dynamic reversibility. The corresponding mechanism diagram is shown in Fig. 1. Consequently, a superior recoverable W_{rec} of 6.11 J/cm³ and an impressive η of 86% are achieved at an E_b of 330 kV/cm in the $0.98(BNSB)_{0.985}S_{0.01}T$–0.02CMN ceramics, together with excellent temperature, frequency, dielectric, and charge-discharge properties. These results demonstrate that the $0.98(BNSB)_{0.985}S_{0.01}T$–0.02CMN ceramics have great potential for practical applications in next-generation pulse power devices and systems.

2 Experimental

2.1 Material synthesis

BNT-based ceramic compositions $(1-x)(0.7Bi_{0.5}Na_{0.5}TiO_3$–$0.3Ba_{0.3}Sr_{0.7}TiO_3)$–$xCa(Mg_{1/3}Nb_{2/3})O_3$ (denoted as (1–*x*)(BNT–SBT)–*x*CMN) with x = 0, 0.02, 0.05, and 0.08) and 0.98 $(Bi_{0.35}Na_{0.35}Sr_{0.21}Ba_{0.09})_{1-1.5y}Sm_yTiO_3$–$0.02Ca(Mg_{1/3}Nb_{2/3})O_3$) (denoted as $(BNSB)_{1-1.5y}S_yT$–0.02CMN with y = 0, 0.01, and 0.015) were fabricated by a conventional solid-state reaction method. The raw materials Na_2CO_3 (99.9%), Bi_2O_3 (99.9%), $SrCO_3$ (99.0%), Sm_2O_3 (99.0%), $BaCO_3$ (99.0%), Nb_2O_5 (99.9%), TiO_2 (99.9%), and MgO (99.0%) were purchased from Aladdin. After an appropriate amount of powder was weighed, it was mixed and placed in a ball mill at a speed of 400 r/min for 12 h. The ball-milled samples were placed in a drying oven at 90 °C for 12 h. The dried sample was ground moderately and placed in a crucible for presintering at a temperature of 850 °C for 3 h. The presintered samples were repeatedly ball milled and dried. The best powder obtained is prepressed at a pressure of 2 MPa and then cold isostatic pressed at a pressure of 250 MPa for 10 min. Final sintering was conducted in air at temperatures of approximately 1130–1150 °C for a dwell time of 3 h.

2.2 Characterizations

The crystalline structure was analysed by X-ray diffraction (XRD; Bruker D8 ADVANCE). Microstructural examination and grain size analysis were performed on thermally etched surfaces (FE-SEM; Zeiss Gemini SEM 300). The elemental distribution was verified via energy dispersive spectroscopy (EDS) coupled with a scanning electron microscope (SEM). The local structural evolution is measured by transmission electron microscopy (TEM; JEM-2100F). The local polarization behavior and domain

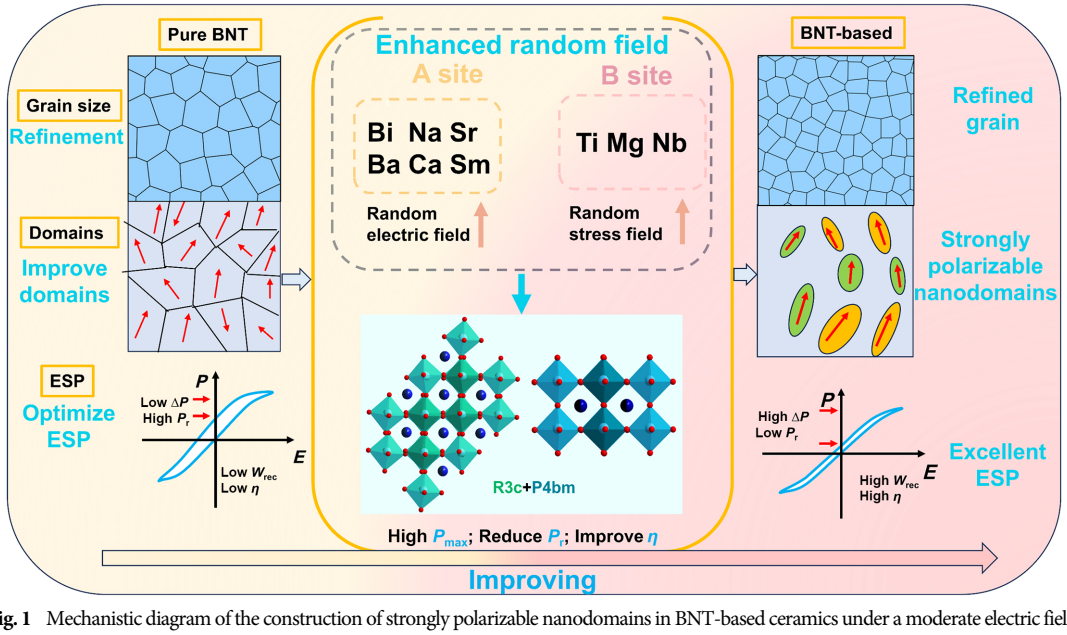

Fig. 1 Mechanistic diagram of the construction of strongly polarizable nanodomains in BNT-based ceramics under a moderate electric field.

structures were investigated at the nanoscale by piezoresponse force microscopy (PFM; Asylum Research MFP-3D). The dielectric permittivity and loss were measured by an LCR meter (DPTS-3000, Wuhan Yanhe Technology Co., Ltd., China). (*P*–*E*) hysteresis loops and E_b were acquired by a standardized ferroelectric test system (PolyK Technologies; sample thickness, 50 μm; electrode diameter, 0.5 mm; testing frequency, 10 Hz). The charge–discharge performance was assessed by a CFD-003.

3 Results and discussion

On the basis of the aforementioned experimental design idea, $(1-x)(0.7Bi_{0.5}Na_{0.5}TiO_3-0.3Ba_{0.3}Sr_{0.7}TiO_3)-xCa(Mg_{1/3}Nb_{2/3})O_3$ (denoted as $(1-x)$(BNT–SBT)–xCMN) ceramics with x = 0, 0.02, 0.05, and 0.08) were synthesized. To further enhance local structural heterogeneity and improve electrical properties, the optimal component (x = 0.02) was modified by Sm^{3+} doping, yielding the $(BNSB)_{1-1.5y}S_yT$–0.02CMN series [37]. The optimal Sm^{3+} content was determined to be y = 0.01, corresponding to the sample that exhibited the best performance.

Figure. 2(a) and Fig. S1 in the Electronic Supplementary Material (ESM) show the XRD patterns of $(1-x)$(BNT–SBT)–xCMN and $(BNSB)_{1-1.5y}S_yT$–0.02CMN ceramic samples at room temperature. All the samples exhibit a typical single-phase perovskite structure (PDF#89-3019) without obvious secondary phases, indicating that all the doped cations were successfully incorporated into the BNT lattice [38,39]. As illustrated in Fig. 2(b), the (200) peak shifts toward lower angles with the introduction of doped ions, indicating lattice expansion. Specifically, the smaller A-site ions Na^+ (1.39 Å) and Bi^{3+} (1.38 Å) are partially replaced by larger Ba^{2+} (1.61 Å) and Sr^{2+} (1.44 Å) ions, whereas the larger B-site cations Nb^{5+} (0.64 Å) and Mg^{2+} (0.72 Å) are substituted for Ti^{4+} (0.604 Å), as shown in Fig. 2(c) [40]. Furthermore, the magnified XRD patterns clearly show splitting of the (200)/(002) diffraction peaks, demonstrating the coexistence of the *R* phase and *T* phase structures in these ceramics. Such *R*–*T* phase coexistence is beneficial for forming strongly polarizable nanodomains, suppressing polarization hysteresis, and consequently optimizing the ESP [41,42]. Rietveld refinements of the $(BNSB)_{1-1.5y}S_yT$–0.02CMN ceramics using the *R3c* and *P4bm* models (Figs. 2(d)–2(f)) show excellent agreement between the calculated and observed XRD profiles, indicating that the fitting results are reliable. The refined parameters are listed in Table S1. As the Sm^{3+} content increases from y = 0 to 0.015, the *R*/*T* phase fraction increases from approximately 35 : 65 to 77 : 23, indicating that Sm^{3+} stabilizes the *R* phase while suppressing the *T* phase. The optimized *R*/*T* phase plays a decisive role: the coexistence of *R*/*T* phases reduces the polarization anisotropy and significantly lowers the energy barrier for polarization rotation near structural boundaries, leading to abnormally high polarizability. This intrinsic mechanism underpins the formation of strongly polarizable nanodomains [43].

To elucidate the impact of compositional changes and Sm^{3+} doping on the microstructure, the surface morphologies of the $(1-x)$(BNT–SBT)–xCMN and $(BNSB)_{1-1.5y}S_yT$–0.02CMN samples were examined by SEM (Figs. 3(a)–3(c) and Figs. S2(a)–S2(c) in the ESM). SEM micrographs revealed densely packed microstructures with clearly defined grain boundaries and minimal porosity for all the samples. In addition, no abnormal grain growth or secondary phases are observed, indicating

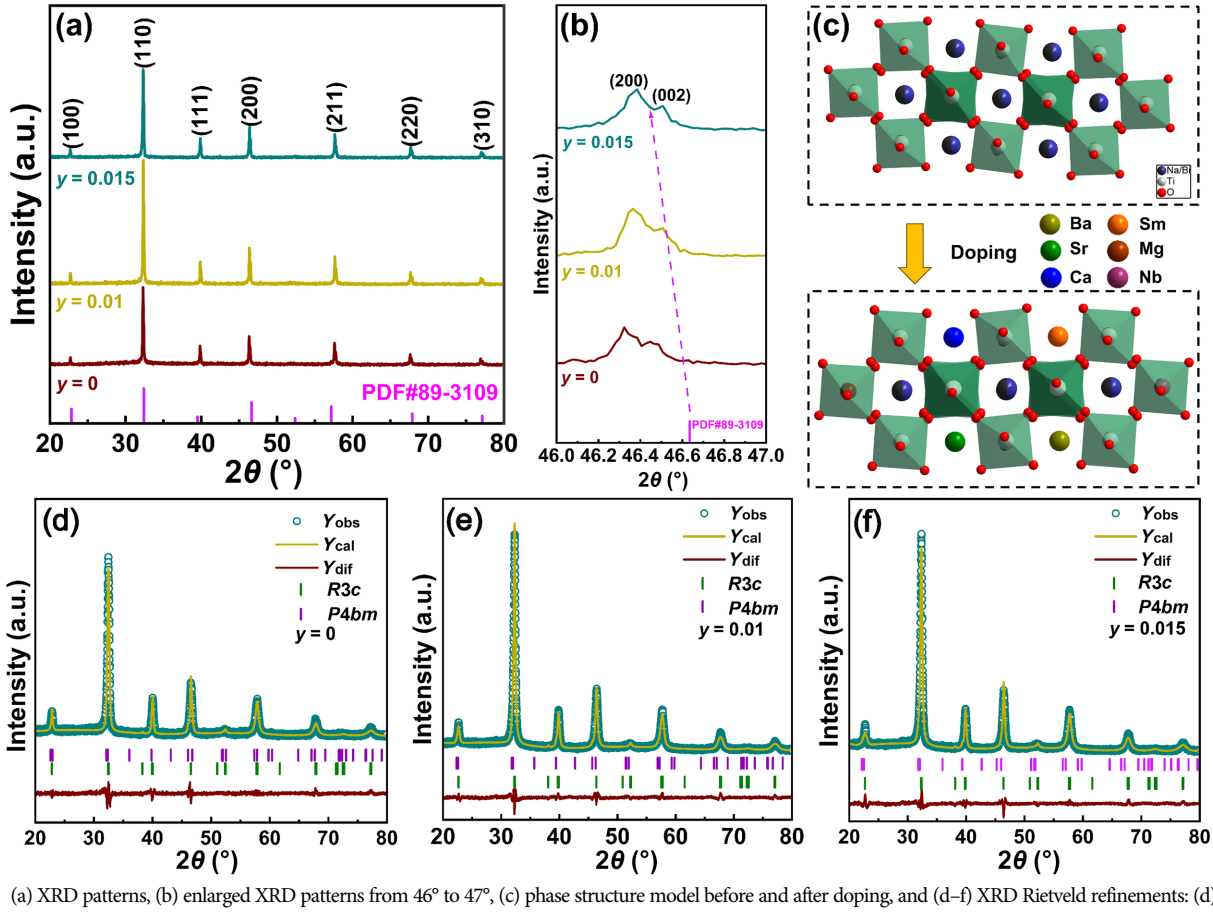

Fig. 2 (a) XRD patterns, (b) enlarged XRD patterns from 46° to 47°, (c) phase structure model before and after doping, and (d–f) XRD Rietveld refinements: (d) y = 0, (e) y = 0.01, and (f) y = 0.015 for $(BNSB)_{1-1.5y}S_yT$–0.02CNN ceramics.

excellent sintering quality and phase purity, which is consistent with the XRD data. The grain sizes of the (1–x)(BNT–SBT)–xCMN ceramics range from 0.47–0.69 μm (Figs. S2(d)–S2(f) in the ESM). The average grain size decreased notably with Sm^{3+} incorporation, from approximately 0.47 μm for the undoped sample to approximately 0.28 μm for y = 0.015 (Figs. 3(d)–3(f)), primarily because of the solute drag effect and lattice distortion induced by Sm^{3+}, which inhibited grain boundary migration during sintering. This grain refinement mechanism, attributed to solute drag and lattice distortion induced by aliovalent doping, has been widely observed in BNT-based perovskite systems [44].

According to the relation $E_b = 1/\sqrt{G}$ (G is the average grain size), grain refinement enhances E_b by increasing the grain-boundary density, thereby impeding charge transport and reducing the leakage current and dielectric loss [45]. Compared with previously reported BNT-based ceramics, the present samples exhibit finer grains. This result is ascribed to both induced lattice strain and suppressed ion diffusion from multi-ion substitution $(Mg_{1/3}Nb_{2/3})^{4+}$ for Ti^{4+} and Sm^{3+} replacing volatile Bi^{3+}/Na^{+}, which reduces oxygen vacancies and limits grain coarsening [46–48]. On the other hand, the relatively low sintering temperature and short dwell time further restrain grain growth [49]. Furthermore, the EDS mapping results reveal a uniform elemental distribution within the representative sample with y = 0.01, as shown in Fig. 3(g). Overall, the dense microstructure, refined grains, and compositional homogeneity synergistically increase the dielectric insulation strength and breakdown strength, thereby providing a solid structural foundation for the superior ESP.

Given the unique phase composition and fine-grained morphology, the dielectric characteristics of the ceramics were further investigated. The ε_r and tanδ of (1–x)(BNT–SBT)–xCMN and $(BNSB)_{1-1.5y}S_yT$–0.02CMN ceramics measured from 30 to 400 °C are shown in Figs. 4(a)–4(c) and Fig. S3 in the ESM,

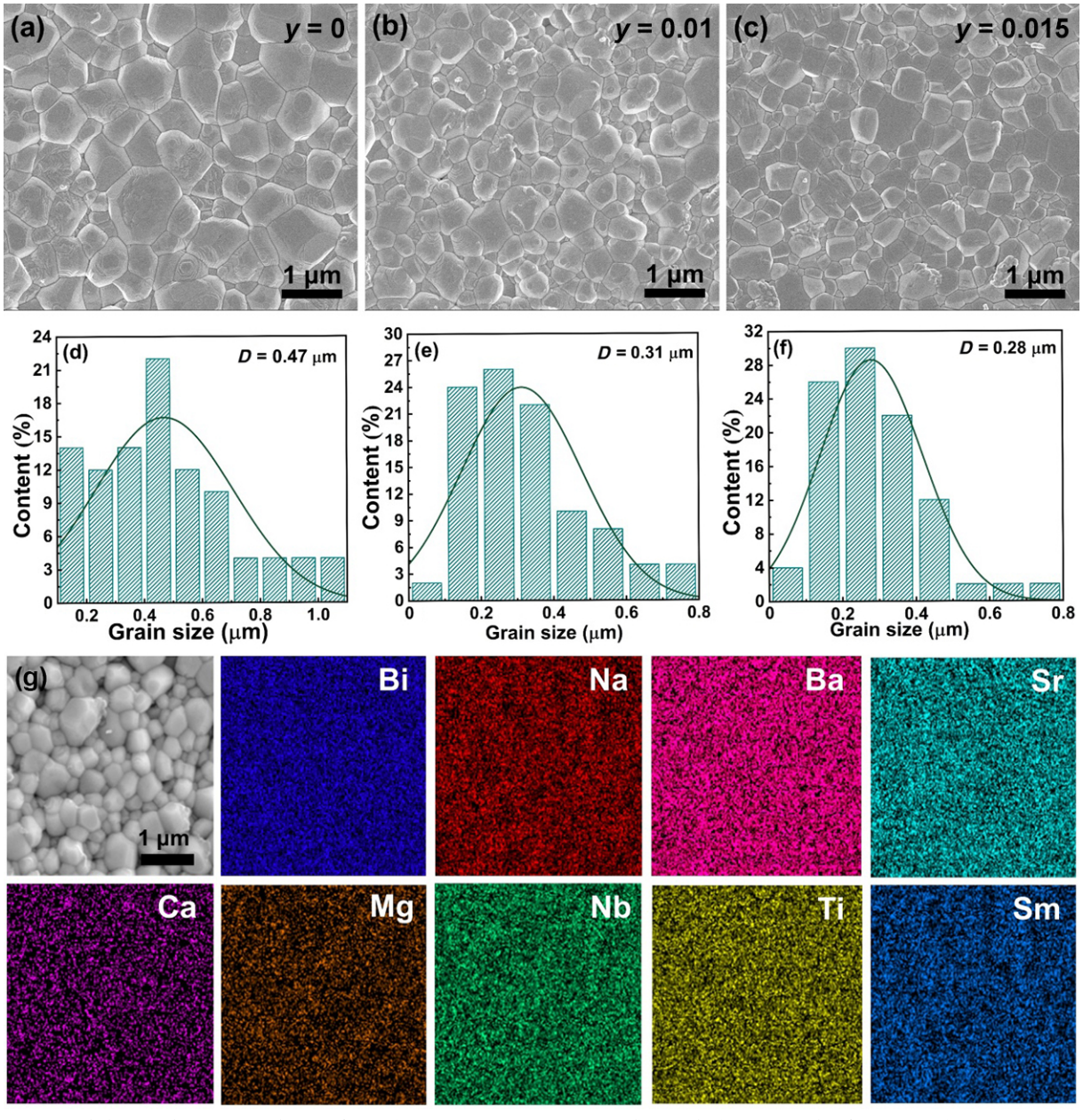

Fig. 3 SEM morphologies with grain size and mean of $(BNSB)_{1-1.5y}S_yT$–0.02CMN ceramics: (a, d) y = 0, (b, e) y = 0.01, and (c, f) y = 0.015; (g) EDS mapping images of $(BNSB)_{1-1.5y}S_yT$–0.02CMN ceramic with y = 0.01.

respectively. All ceramics exhibit a broad dielectric anomaly near the temperature (T_m which presents the maximum of ε_r), which arises from the synergistic effects of the *R*–*T* phase transition and the thermal evolution of tetragonal polar nanodomains [50,51]. As the frequency increases from 1 kHz to 1 MHz, the dielectric peaks progressively broaden, reflecting the typical frequency dispersion of relaxor ferroelectrics caused by local random electric fields that disturb long-range ferroelectric ordering [52,53]. Compared with the undoped sample (y = 0), the Sm^{3+}-modified ceramics have a slightly lower maximum permittivity but a much greater improvement in thermal stability. This reduction in ε_r results from enhanced local lattice distortion and random fields induced by Sm^{3+} substitution, which weaken long-range correlations while promoting the formation of dynamic PNRs. Consequently, these ceramics exhibit stronger relaxor characteristics and suppressed dielectric loss, with tanδ remaining below 0.02 across 25–350 °C. These results demonstrate that Sm^{3+} doping effectively stabilizes the dielectric response, suppresses conduction loss, and provides the thermal and electrical robustness essential for obtaining reliable ESPs at moderate electric fields.

To further evaluate the dielectric stability, the temperature-dependent dielectric spectra of $(BNSB)_{1-1.5y}S_yT$–0.02CMN ceramics at 1 kHz were obtained, as shown in Fig. 4(d). With increasing Sm^{3+} content, the dielectric peak at T_m gradually decreases, whereas the T_m position remains nearly unchanged, indicating that Sm^{3+} substitution has little influence on the Curie temperature and phase transition behavior. The slight increase in tanδ at elevated temperatures is attributed to thermally activated leakage and defect conduction. The temperature coefficient of the dielectric constant (TCP), which is calculated according to Eq. (4) [54], where the dielectric constant at 200 °C ($\varepsilon_{200\,°C}$) is used as the reference benchmark, is shown in Fig. 4(e):

$$\mathrm{TCP} = (\varepsilon_r - \varepsilon_{200\,°C})/\varepsilon_{200\,°C} \tag{4}$$

The light green region (TCP ≤ ±10%) represents the temperature range of the stable dielectric response. The undoped sample exhibits a sharp increase in ε_r between 75 and 170 °C, exceeding ±10%, whereas Sm^{3+} doped ceramics maintain a nearly constant dielectric constant (TCP ≤ ±10%) from 50 to 250 °C. The similar stability of the y = 0.01 and 0.015 samples results from their comparable Sm^{3+} content. This improved dielectric stability originates from the optimized *R*/*T* phase proportion and enhanced relaxation of the PNRs, which together suppress temperature-induced polarization fluctuations. Therefore, Sm^{3+} doping effectively broadens the temperature range of dielectric stability, providing robust dielectric reliability crucial for practical high-temperature energy storage capacitors.

To gain a deeper understanding of the relaxation characteristics of the $(BNSB)_{1-1.5y}S_yT$–0.02CMN ceramics, the degree of dispersion in their phase transition was quantified by applying the modified Curie–Weiss law to determine the diffuseness exponent (γ) (Eq. (5)):

$$\frac{1}{\varepsilon_r} - \frac{1}{\varepsilon_m} = \frac{(T - T_m)^{\gamma}}{C} \tag{5}$$

where ε_r is the dielectric constant, ε_m is the maximum value of dielectric constant, and C is the Curie constant, respectively. The diffuseness coefficient (γ) typically falls within the range of 1 to 2. A value of γ = 1 signifies normal ferroelectric behavior, whereas γ = 2 represents an ideal relaxor state. The plots of $\ln(1/\varepsilon_r - 1/\varepsilon_m)$ against $\ln(T - T_m)$ measured at 1 kHz, along with the derived γ values, are shown in Fig. 4(f). The γ value initially increases with increasing Sm^{3+} content, followed by a slight decrease, suggesting that the relaxor characteristics are most pronounced at intermediate doping concentrations. This trend stems from the substitution of Sm^{3+} ions, which disrupts long-range ferroelectric order through the introduction of random fields and ionic mismatch, thereby fostering the development of PNRs. Consequently, the augmented relaxation behavior promotes easier polarization reversal, which in turn supports higher η under moderate electric fields.

To clarify the underlying local structural evolution responsible for these properties, TEM and selected area electron diffraction (SAED) analyses were carried out on the y = 0.01 ceramic, as shown in Fig. 5 and Fig. S4 in the ESM. The TEM images (Fig. 5(a) and Fig. S4(a) in the ESM) reveal distinct dark contrast

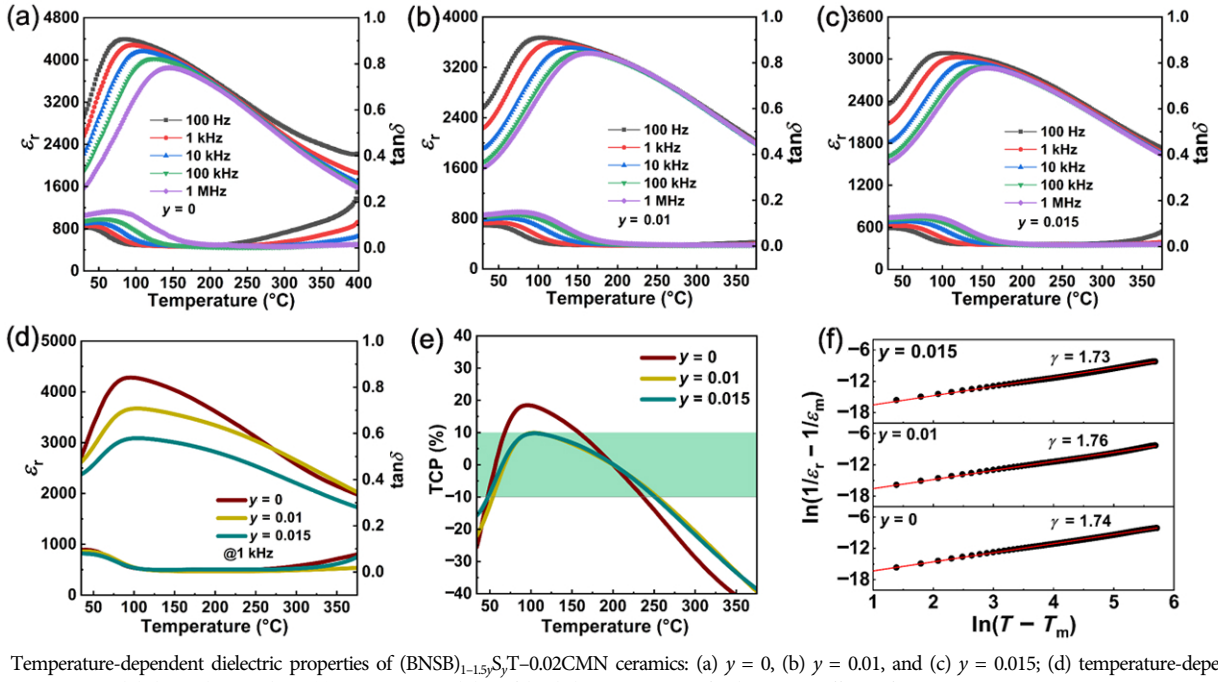

Fig. 4 Temperature-dependent dielectric properties of $(BNSB)_{1-1.5y}S_yT$–0.02CMN ceramics: (a) y = 0, (b) y = 0.01, and (c) y = 0.015; (d) temperature-dependent dielectric constant and dielectric loss at 1 kHz; (e) temperature stability of the dielectric constant; (f) relaxation coefficient fitting.

清華大学出版社 Tsinghua University Press | SciOpen

regions, corresponding to strongly polarizable domain structures. High-resolution TEM images (Fig. 5(b) and Fig. S4(b) in the ESM) reveal numerous nanoscale dark stripes of varying sizes, which can be attributed to the polar nanodomain characteristics of relaxor ferroelectrics [55]. The SAED patterns further confirm the coexistence of multiple structural modulations: 1/2(*ooo*) superlattice reflections are observed along the $[110]_c$ zone axis (Fig. 5(e)), corresponding to the antiphase $a^-a^-a^-$ octahedral tilts associated with the *R3c* symmetry [56], whereas 1/2(*ooe*) reflections along $[001]_c$ (Fig. 5(f)) arise from the in-phase $a^0a^0c^+$ tilts typical of the *P4bm* structure [57]. The nanoscale band contrast in the TEM image revealed the formation of strongly polarizable nanodomains, resulting from the coexistence of *R* and *T* phases, which was also revealed by the XRD data and TEM SAED patterns of the $y = 0.01$ ceramic.

To gain deeper insight into the microscopic polarization dynamics and domain evolution within the $(BNSB)_{1-1.5y}S_yT$–0.02CMN ceramics, PFM measurements were performed. The resulting PFM amplitude and phase images for compositions with $y = 0$ and 0.01 are presented in Fig. 6 and Fig. S5 in the ESM. The phase contrast in these images is indicative of domain orientation switching, whereas the amplitude contrast is directly correlated with the local piezoelectric response strength. Analysis of Fig. 6(b) and Fig. S5(b) in the ESM reveals that the undoped ceramic ($y = 0$) displays extensive regions with strong, uniform piezoresponse contrast. This pattern is characteristic of a well-defined, long-range ferroelectric domain structure. In contrast, the Sm^{3+}-doped ceramic ($y = 0.01$) displays fine, alternately bright and dark regions (Fig. 6(d) and Fig. S5(d) in the ESM), revealing the fragmentation of macroscopic domains into nanoscale polar regions. The fine, alternating contrast in PFM phase/amplitude reflects highly dynamic PNRs capable of rapid reversal under external fields, supporting both strong polarizability and low hysteresis. These domains are consistent with the TEM observations and are characteristic of relaxor-type behavior in BNT-based systems. The emergence of these polar nanodomains enhances local field fluctuations and increases the threshold field for polarization reversal, contributing to the formation of a slim *P*–*E* loop. Therefore, the PFM results demonstrate that Sm^{3+}-induced transformation from long-range ferroelectric domains to highly dynamic PNRs is essential for constructing strongly polarizable nanodomains and achieving superior ESPs. These features between TEM and PFM collectively underpin the high P_{max} and low P_r observed macroscopically, confirming the "strong polarity" and "dynamic reversibility" of the engineered nanodomains.

The electric field-dependent polarization behavior and breakdown strength are vital for enhancing the ESP reliability of dielectric ceramics. The Weibull distribution of all the samples is linear, confirming the measurement reliability and uniform microstructure (Fig. 7(a) and Fig. S6(a) in the ESM). Notably, the sample with $y = 0.01$ presents the highest E_b of 330 kV/cm because of the suppressed local field concentration and strong breakdown resistance induced by grain refinement and reduced defect

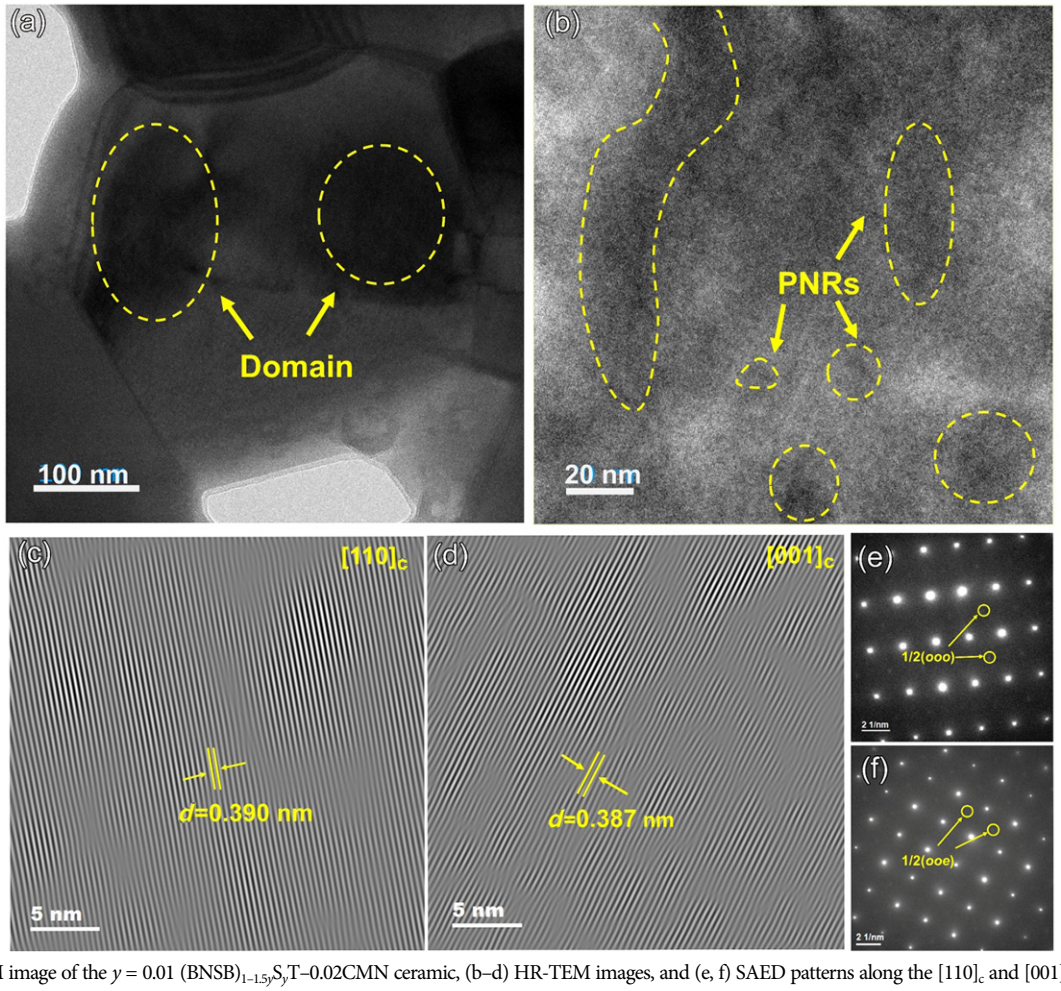

Fig. 5 (a) TEM image of the $y = 0.01$ $(BNSB)_{1-1.5y}S_yT$–0.02CMN ceramic, (b–d) HR-TEM images, and (e, f) SAED patterns along the $[110]_c$ and $[001]_c$ of the $y = 0.01$ $(BNSB)_{1-1.5y}S_yT$–0.02CMN ceramic.

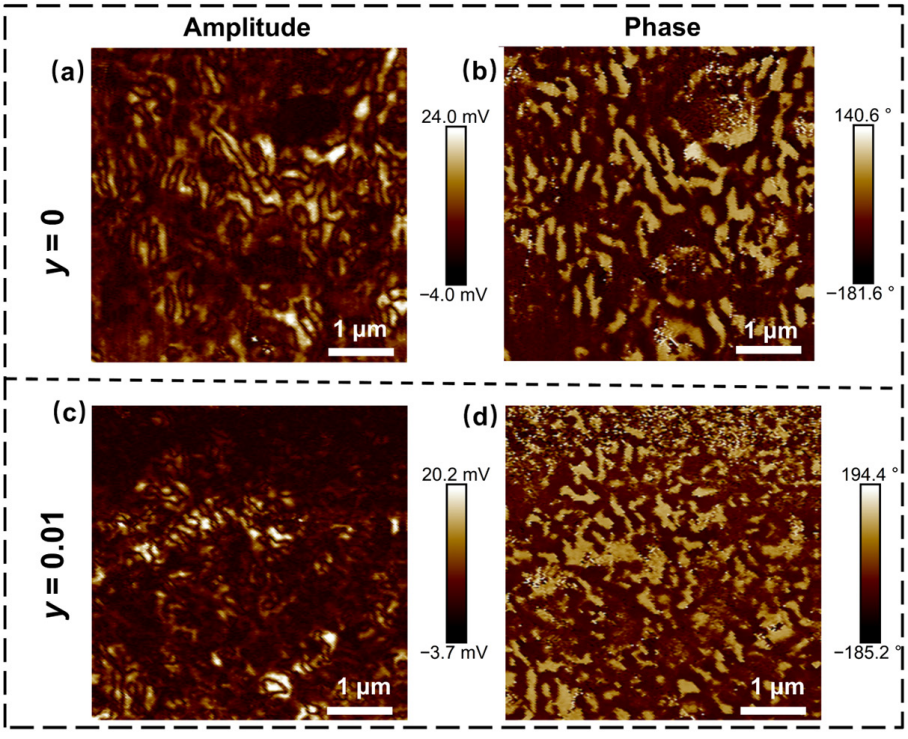

Fig. 6 (a, c) PFM amplitude and (b, d) phase images of the $y = 0$ and 0.01 $(BNSB)_{1-1.5y}S_yT$–0.02CMN ceramic samples.

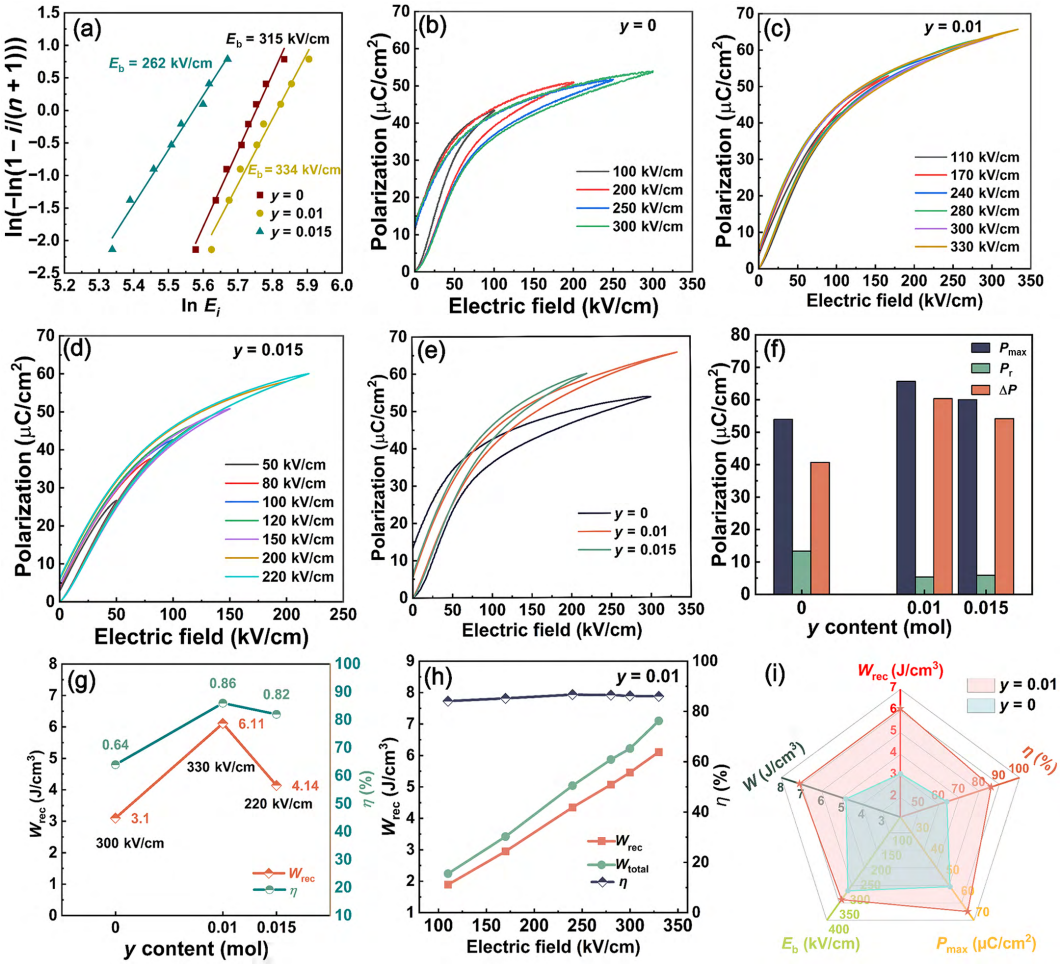

Fig. 7 (a) Weibull distribution of E_b. Unipolar P–E curves under different electric fields of $(BNSB)_{1-1.5y}S_yT$–0.02CMN ceramic samples ((b) $y = 0$, (c) $y = 0.01$, and (d) $y = 0.015$. (e) Respective P–E loops under the highest electric field. (f) Corresponding P_{max}, P_r and P_{max}–P_r values. (g) W_{rec}, η of $(BNSB)_{1-1.5y}S_yT$–0.02CMN ceramics. (h) W_{rec} and η of $y = 0.01$ $(BNSB)_{1-1.5y}S_yT$–0.02CMN at different electric fields. (i) Performance radar chart of $(BNSB)_{1-1.5y}S_yT$–0.02CMN ceramic samples ($y = 0$ and 0.01).

density. As shown in Fig. S6(b) in the ESM, the unipolar *P*–*E* loops of the (1–*x*)(BNT–SBT)–*x*CMN ceramics at room temperature indicate that the $x = 0.02$ sample exhibits a slim *P*–*E* loop with a higher P_{max} and E_b, resulting in a higher W_{rec} of approximately 3.1 J/cm³ at 300 kV/cm but an inferior η, as displayed in Fig. S6(c) in the ESM.

To further enhance the comprehensive ESP, Sm^{3+} was incorporated into the 0.98(BNT–SBT)–0.02CMN system to strengthen the local structural heterogeneity. On the basis of the rational component design, the $(BNSB)_{1-1.5y}S_yT$–0.02CMN ceramics with strongly polarizable nanodomains display superior ESPs. The unipolar *P*–*E* loops of $(BNSB)_{1-1.5y}S_yT$–0.02CMN ceramics were systematically examined under various electric fields, as depicted in Figs. 7(b)–7(e). The sample with $y = 0.01$ has notably slim *P*–*E* loops accompanied by a higher E_b. This composition has a significantly higher $P_{max} = 65.8$ μC/cm² and a lower $P_r = 5.34$ μC/cm², as shown in Figs. S6(d)–S6(f) in the ESM. Impressively, the $y = 0.01$ sample has the highest W_{rec} of 6.11 J/cm³ and an η of 86% at a moderate electric field of 330 kV/cm (Fig. 7(g)). Moreover, as illustrated in Fig. 7(h), the P_r of the $y = 0.01$ sample remains nearly invariant with increasing electric field, whereas the polarization increases almost linearly, thereby ensuring high and stable η over a broad field range. The ultrahigh polarization originates from the formation of strongly polarizable nanodomains, and the slim hysteresis with a low P_r of the $y = 0.01$ sample confirms that the coexistence of PNRs and multiphase nanodomains can effectively suppress domain back-switching. Overall, all key parameters related to the ESP of the $y = 0.01$ and 0 ceramics are summarized in Fig. 7(i). Compared with the $y = 0$ ceramic, the $y = 0.01$ ceramic has a higher E_b and a larger P_{max}, endowing this ceramic with a superior comprehensive ESP (higher W_{rec} and η) and demonstrating great potential under a moderate electric field for use in dielectric capacitors.

To demonstrate the achievements of our BNT-based ceramic system, a comparison of P_{max}, W_{rec}, and η with other currently reported lead-free dielectric ceramics under comparable electric fields is given in Fig. 8. Figure. 8(a) shows that the $y = 0.01$ ceramic exhibits a higher P_{max} of 65.8 μC/cm² under moderate electric field than that of other bulk dielectric ceramics [58–70]. More importantly, compared with the vast majority of reported bulk ceramics tested at comparable electric fields, the $y = 0.01$ ceramic presents a larger W_{rec} of 6.11 J/cm³ and a higher η of 86% at 330 kV/cm (Fig. 8(b)) [46,58,60,61,64,71,72]. Notably, while many previously reported systems achieve either high W_{rec} or high η, they often compromise the other parameters. In contrast, our optimized composition uniquely achieves both high W_{rec} (6.11 J/cm³) and high η (86%), representing a significant advancement in the comprehensive ESP. Collectively, these findings demonstrate that engineering strongly polarizable nanodomains presents a viable strategy for increasing the ESP of lead-free dielectrics under moderate electric fields. The optimized $(BNSB)_{1-1.5y}S_yT$–0.02CMN composition, a direct outcome of this approach, is consequently positioned as a foremost candidate for high-performance capacitors in such operational regimes.

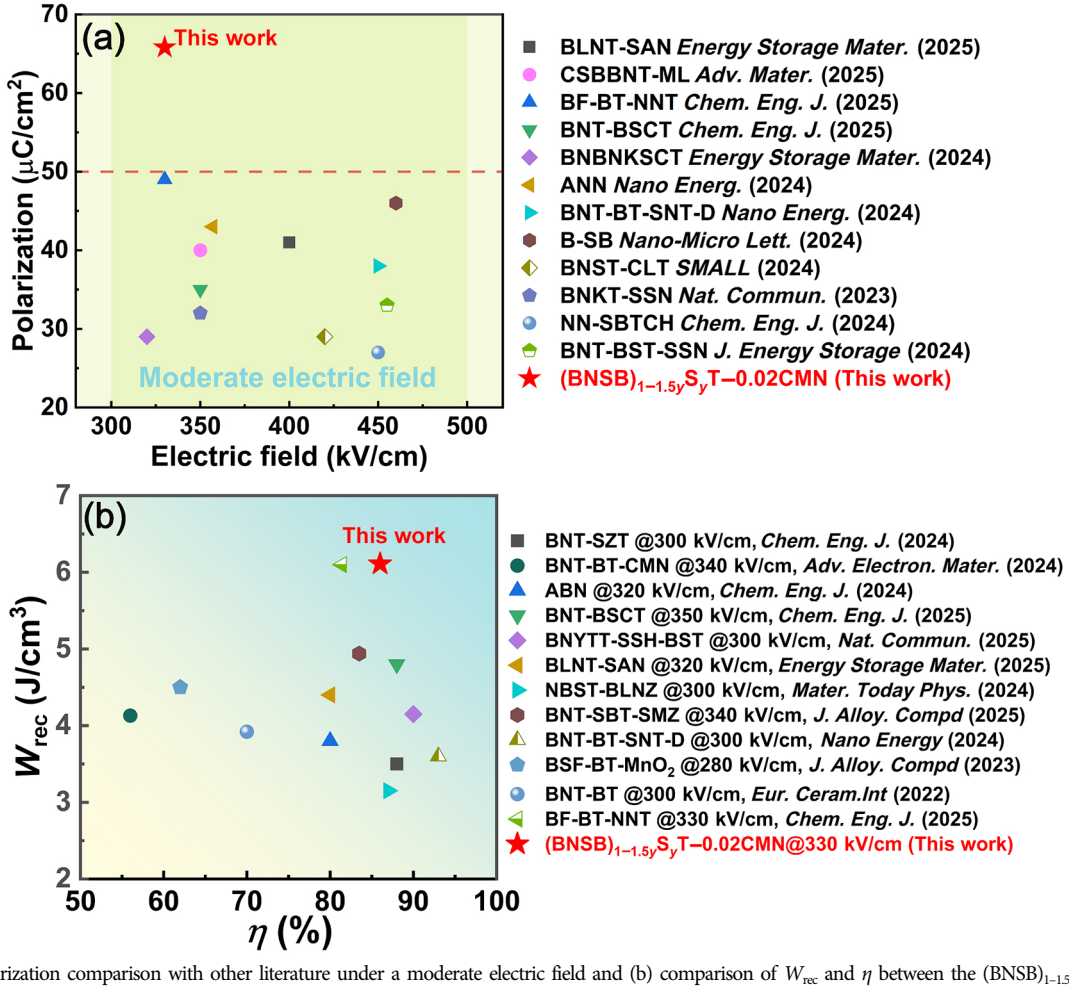

Fig. 8 (a) Polarization comparison with other literature under a moderate electric field and (b) comparison of W_{rec} and η between the $(BNSB)_{1-1.5y}S_yT$–0.02CMN ceramic in this work and other energy storage ceramics near the field of 330 kV/cm.

Excellent temperature and frequency stability are key material properties enabling the real-world use of dielectric ceramic capacitors across diverse operating conditions. To evaluate these properties, the *P*–*E* loops were measured from 20 to 140 °C under 150 kV/cm, as shown in Figs. 9(a) and 9(b). Notably, both P_{max} and P_r show minimal variation with increasing temperature, corresponding to a slight fluctuation in W_{rec} between 2.0 and 2.5 J/cm³. Moreover, η remains nearly constant at ~80%, confirming the excellent thermal stability and reliable energy storage capability of the y = 0.01 sample. The frequency-dependent ESP was also investigated, with *P*–*E* loops measured from 5 to 500 Hz (Figs. 9(c) and 9(d)). The loops maintain their slim shape across the frequency range, and P_{max} and P_r exhibit negligible changes. The W_{rec} of the y = 0.01 composition remains between 2.2 and 2.5 J/cm³, while the η remains above 80%, demonstrating outstanding frequency stability.

Furthermore, the evaluation of pulse charge-discharge behavior is integral to assessing the practical viability of dielectric capacitors. Representative overdamped discharge current waveforms acquired under electric fields varying from 40 to 200 kV/cm are displayed in Fig. 9(e), wherein the peak current consistently increases with increasing applied field strength. The discharge energy density can be further evaluated by $W_d = R\int I^2(t)dt/V$, where R is the load resistance (1000 Ω), and V is the effective volume of the tested samples [73]. As shown in Fig. 9(f), the value of W_d increased from 0.20 to 2.45 J/cm³ with a discharge time

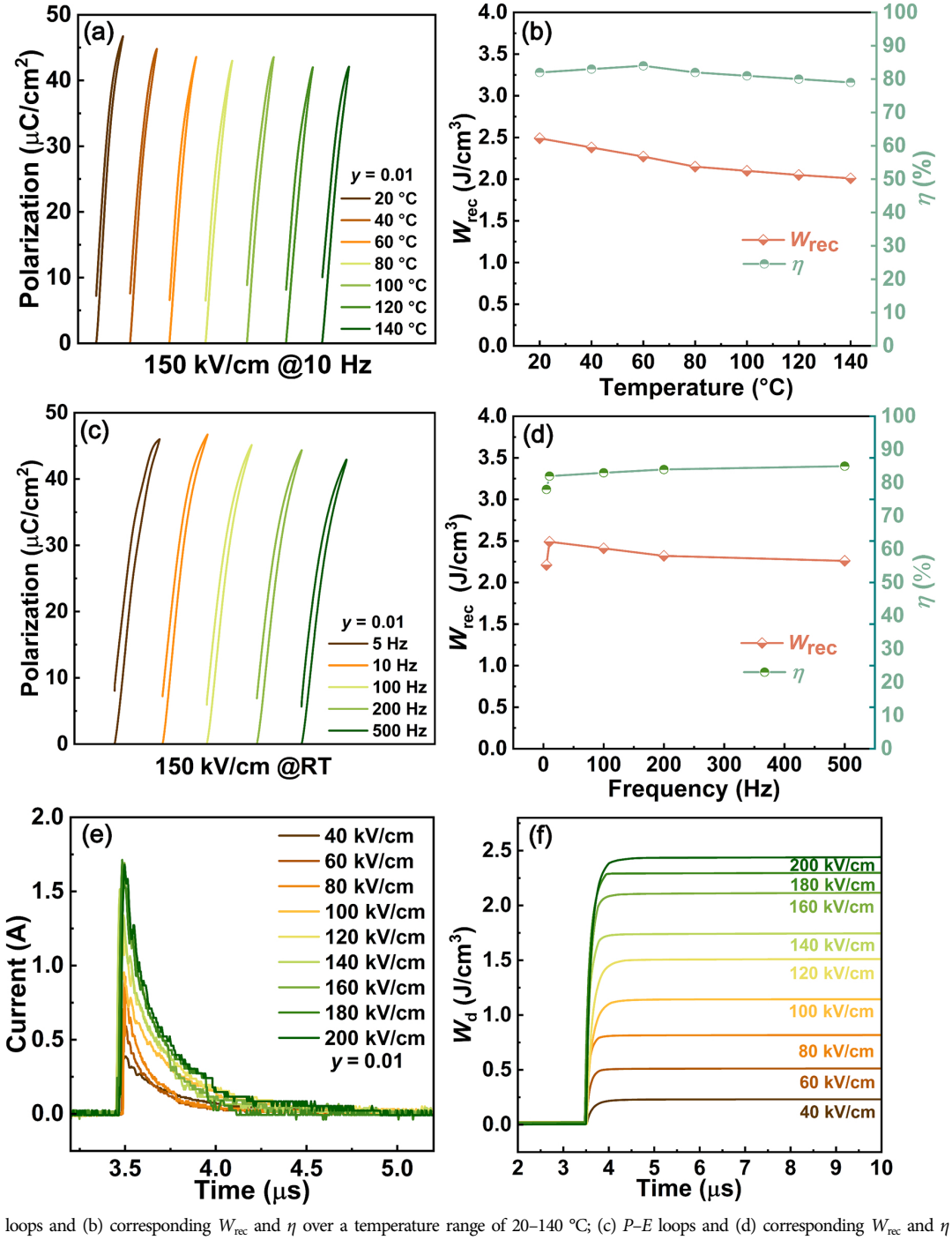

Fig. 9 (a) *P*–*E* loops and (b) corresponding W_{rec} and η over a temperature range of 20–140 °C; (c) *P*–*E* loops and (d) corresponding W_{rec} and η of 5–500 Hz; (e) overdamped charge-discharge curves and (f) discharge energy density under the corresponding field of y = 0.01 $(BNSB)_{1-1.5y}S_yT$–0.02CMN ceramic.

$\tau_{0.9}$ ≈ 3.7 μs (time to release 90% of the electric energy) when the electric field increased from 40 to 200 kV/cm, revealing rapid and efficient energy release within a practical electric circuit. Building upon these performance parameters, an integrated assessment confirms the great potential of the $(BNSB)_{0.985}S_{0.01}T$–0.02CMN ceramic for capacitor applications in moderate electric fields. Its suitability stems from a combination of high energy storage capacity, exceptional stability across wide temperature and frequency ranges, and efficient charge-discharge performance.

4 Conclusions

In summary, we propose and validate a strategy centered on constructing strongly polarizable nanodomains. This is achieved by rationally designing local structural heterogeneity and optimizing the ratio of coexisting *R* and *T* phases through multi-ion substitution. The resulting enhanced random field disrupts long-range ferroelectric order, reduces polarization anisotropy, significantly lowers the energy barrier for polarization rotation near structural boundaries, and forms strongly polarizable nanodomains, yielding highly dynamic PNRs that enable ultrahigh P_{max}. Concurrently, the optimized phase composition promotes the formation of ultrafine grains and a dense microstructure, which effectively reduces P_r and increases E_b. As a result of the combination of ultrahigh polarization and low P_r, the developed BNT-based ceramics demonstrate outstanding ESP, attaining a W_{rec} of 6.11 J/cm^3 with an η of 86% at 330 kV/cm. This represents a significant advancement over other ceramic counterparts tested under comparable electric field conditions. Furthermore, these ceramics possess remarkable stability against temperature and frequency variations, along with robust dielectric properties and superior charge-discharge characteristics, underscoring their strong potential for deployment in advanced pulse-power systems. Consequently, this study establishes a viable and effective design strategy for achieving ultrahigh comprehensive ESPs in lead-free ceramics operating under moderate electric fields.

Acknowledgements

This study was financially supported by the National Natural Science Foundation of China (Nos. 52202136 and 52562019), the Natural Science Foundation of Jiangxi Province (No. 20232BAB204017), the State Key Laboratory of Electrical Insulation and Power Equipment (No. EIPE24203), the Guangdong Provincial Key Laboratory of Electronic Functional Materials and Devices (No. EFMD2024002Z), the China National Postdoctoral Program for Innovative Talents (No. BX20240035), the China Postdoctoral Science Foundation (No. 2024M760202), and the Graduate Innovation Special Fund of Jiangxi Province (No. YC2024-S607).

Availability of data and materials

The data that support the findings of this study are available from the corresponding author upon reasonable request.

Competing interests

The authors have no competing interests to declare that are relevant to the content of this article.

References

[1] Guney MS, Tepe Y. Classification and assessment of energy storage systems. *Renew Sustain Energy Rev* 2017, **75**: 1187–1197.
[2] Liu C, Li F, Ma LP, *et al.* Advanced materials for energy storage. *Adv Mater* 2010, **8**: 28–62.
[3] Chen HS, Cong TN, Yang W, *et al.* Progress in electrical energy storage system: A critical review. *Prog Nat Sci* 2009, **19**: 291–312.
[4] Pan H, Li F, Liu Y, *et al.* Ultrahigh–energy density lead-free dielectric films via polymorphic nanodomain design. *Science* 2019, **365**: 578–582.
[5] Pan H, Ma J, Ma J, *et al.* Giant energy density and high efficiency achieved in bismuth ferrite-based film capacitors via domain engineering. *Nat Commun* 2018, **9**: 1813.
[6] Wang G, Lu ZL, Li Y, *et al.* Electroceramics for high-energy density capacitors: Current status and future perspectives. *Chem Rev* 2021, **121**: 6124–6172.
[7] Luo H, Zhou XF, Ellingford C, *et al.* Interface design for high energy density polymer nanocomposites. *Chem Soc Rev* 2019, **48**: 4424–4465.
[8] Qi H, Xie AW, Zuo RZ. Local structure engineered lead-free ferroic dielectrics for superior energy-storage capacitors: A review. *Energy Storage Mater* 2022, **45**: 541–567.
[9] Pashnina E, Chezganov D, Slautina A, *et al.* Domain patterning in nonpolar cut PMN-PT by focused ion beam. *J Adv Dielect* 2024, **14**: 2350024.
[10] Zhao PY, Li LT, Wang XH, *et al.* $BaTiO_3$–$NaNbO_3$ energy storage ceramics with an ultrafast charge-discharge rate and temperature-stable power density. *Microstructures* 2023, **3**: 2023002.
[11] He B, Zhou B, Yan SG, *et al.* Ultrahigh energy density and efficiency $BaTiO_3$-based multilayer ceramic capacitors. *J Adv Ceram* 2025, **14**: 9221018.
[12] Qiao XS, Wu D, Zhang FD, *et al.* $Bi_{0.5}Na_{0.5}TiO_3$-based relaxor ferroelectric ceramic with large energy density and high efficiency under a moderate electric field. *J Mater Chem C* 2019, **7**: 10514–10520.
[13] Lv ZQ, Lu T, Liu Z, *et al.* $NaNbO_3$-based multilayer ceramic capacitors with ultrahigh energy storage performance. *Adv Energy Mater* 2024, **14**: 2304291.
[14] Luo NN, Han K, Cabral MJ, *et al.* Constructing phase boundary in $AgNbO_3$ antiferroelectrics: Pathway simultaneously achieving high energy density and efficiency. *Nat Commun* 2020, **11**: 4824.
[15] Zhang M, Yang HB, Lin Y, *et al.* Significant increase in comprehensive energy storage performance of potassium sodium niobate-based ceramics via synergistic optimization strategy. *Energy Storage Mater* 2022, **45**: 861–868.
[16] Liu S, Feng WW, Li JH, *et al.* Achieving high energy storage density and efficiency simultaneously in $Sr(Nb_{0.5}Al_{0.5})O_3$ modified $BiFeO_3$ based lead-free ceramics. *Chem Eng J* 2023, **451**: 138916.
[17] Yan F, He X, Bai HR, *et al.* Excellent energy storage properties and superior stability achieved in lead-free ceramics via a spatial sandwich structure design strategy. *J Mater Chem A* 2021, **9**: 15827–15835.
[18] Pan H, Lan S, Xu SQ, *et al.* Ultrahigh energy storage in superparaelectric relaxor ferroelectrics. *Science* 2021, **374**: 100–104.
[19] Li X, Cheng Y, Wang F, *et al.* Enhancement of energy storage and hardness of $(Na_{0.5}Bi_{0.5})_{0.7}Sr_{0.3}TiO_3$–based relaxor ferroelectrics via introducing $Ba(Mg_{1/3}Nb_{2/3})O_3$. *Chem Eng J* 2022, **431**: 133441.
[20] Jiang MJ, Peng ZH, Zhou QY, *et al.* Superior energy storage performance of BNT-based ferroelectric ceramics based on maintaining high polarization and breakdown strength. *J Adv Dielect* 2024, **14**: 2340005.
[21] Liu Y, Niu RM, Uriach R, *et al.* Coexistence of ferroelectric and ferrielectric phases in ultrathin antiferroelectric $PbZrO_3$ thin films. *Microstructures* 2024, **4**: 2024045.
[22] He S, Lou KJ, Han B, *et al.* Superior energy storage density and efficiency in antiferroelectric-like BNT-based ceramics via single-element phase engineering. *J Adv Ceram* 2025, **14**: 9221056.
[23] Sun ZX, Xin HY, Diwu LM, *et al.* Boosting the energy storage performance of BCZT-based capacitors by constructing a Schottky contact. *Mater Horiz* 2025, **12**: 2328–2340.
[24] Lin J, Wen HL, Feng ZB, *et al.* Anion injection in dielectric

ecosystems to construct dual built-in electric fields for efficient electromagnetic response. *Adv Funct Mater* 2025, **35**: 2505381.
[25] Yang AH, Huan Y, Wang QY, *et al.* Excellent comprehensive piezoelectric performances of SiC-doped BCTZ-based lead-free piezoelectric ceramics. *J Adv Ceram* 2025, **14**: 9221054.
[26] Xu LY, Ouyang J, Cheng ZX, *et al.* A review on the dielectric ceramics for high energy-storage application. *Adv Ceram* 2025, **46**: 195–246.
[27] Qiao XS, Sheng AH, Wu D, *et al.* A novel multifunctional ceramic with photoluminescence and outstanding energy storage properties. *Chem Eng J* 2021, **408**: 127368.
[28] Luo CY, Wei YZ, Feng Q, *et al.* Significantly enhanced energy-storage properties of $Bi_{0.47}Na_{0.47}Ba_{0.06}TiO_3$–$CaHfO_3$ ceramics by introducing $Sr_{0.7}Bi_{0.2}TiO_3$ for pulse capacitor application. *Chem Eng J* 2022, **429**: 132165.
[29] Wang M, Feng Q, Luo CY, *et al.* Ultrahigh energy storage density and efficiency in $Bi_{0.5}Na_{0.5}TiO_3$-based ceramics via the domain and bandgap engineering. *ACS Appl Mater Interfaces* 2021, **13**: 51218–51229.
[30] Yan F, Huang KW, Jiang T, *et al.* Significantly enhanced energy storage density and efficiency of BNT-based perovskite ceramics via A-site defect engineering. *Energy Storage Mater* 2020, **30**: 392–400.
[31] Rawat M, Yadav KL, Kumar A, *et al.* Structural, dielectric and conductivity properties of Ba^{2+} doped $(Bi_{0.5}Na_{0.5})TiO_3$ ceramic. *Adv Mater Lett* 2012, **3**: 286–292.
[32] Yin J, Zhang YX, Lv X, *et al.* Ultrahigh energy-storage potential under low electric field in bismuth sodium titanate-based perovskite ferroelectrics. *J Mater Chem A* 2018, **6**: 9823–9832.
[33] Jing RY, Zhang LY, Hu QY, *et al.* Phase evolution and relaxor to ferroelectric phase transition boosting ultrahigh electrostrains in $(1-x)(Bi_{1/2}Na_{1/2})TiO_{3-x}(Bi_{1/2}K_{1/2})TiO_3$ solid solutions. *J Materiomics* 2022, **8**: 335–346.
[34] Wang ZP, Kang RR, Liu WY, *et al.* $(Bi_{0.5}Na_{0.5})TiO_3$-based relaxor ferroelectrics with medium permittivity featuring enhanced energy-storage density and excellent thermal stability. *Chem Eng J* 2022, **427**: 131989.
[35] Guo J, Yu HF, Ren YF, *et al.* Multi-symmetry high-entropy relaxor ferroelectric with giant capacitive energy storage. *Nano Energy* 2023, **112**: 108458.
[36] Xie AW, Li ZH, Wu X, *et al.* Non-polar nanocluster confinement engineering realizes high capacitive energy storage in Pb-free high-entropy relaxors. *Nat Commun* 2026, **17**: 1584.
[37] Li F, Cabral MJ, Xu B, *et al.* Giant piezoelectricity of Sm-doped $Pb(Mg_{1/3}Nb_{2/3})O_3$–$PbTiO_3$ single crystals. *Science* 2019, **364**: 264–268.
[38] Qiao XS, Zhang FD, Wu D, *et al.* Superior comprehensive energy storage properties in $Bi_{0.5}Na_{0.5}TiO_3$-based relaxor ferroelectric ceramics. *Chem Eng J* 2020, **388**: 124158.
[39] Mao P, Guo YG, Wang T, *et al.* Boosting high electric breakdown strength for excellent energy storage performance in $Bi_{0.5}Na_{0.5}TiO_3$-based lead-free ceramics via a high entropy strategy. *ACS Appl Mater Interfaces* 2025, **17**: 1485–1498.
[40] Mao P, Guo YG, Lu G, *et al.* Synergistic effect of multi-phase and multi-domain structures induced high energy storage performances under low electric fields in $Na_{0.5}Bi_{0.5}TiO_3$-based lead-free ceramics. *Chem Eng J* 2023, **472**: 144973.
[41] Wang Q, Xie B, Zheng QY, *et al.* $Bi_{0.5}Na_{0.5}TiO_3$-based relaxor-ferroelectric ceramics for low-electric-field dielectric energy storage via bidirectional optimization strategy. *Chem Eng J* 2023, **452**: 139422.
[42] Cao WJ, Wu YW, Yang XY, *et al.* Breaking polarization-breakdown strength paradox for ultrahigh energy storage density in NBT-based ceramics. *Nat Commun* 2025, **16**: 6228.
[43] Long CB, Su ZQ, Song HM, *et al.* Excellent energy storage properties with ultrahigh W_{rec} in lead-free relaxor ferroelectrics of ternary $Bi_{0.5}Na_{0.5}TiO_3$–$SrTiO_3$–$Bi_{0.5}Li_{0.5}TiO_3$ via multiple synergistic optimization. *Energy Storage Mater* 2024, **65**: 103055.
[44] Li DX, Deng W, Shen ZY, *et al.* Aliovalent Sm-doping enables BNT-based realxor ferroelectric ceramics with > 90% energy efficiency. *J Adv Ceram* 2024, **13**: 2043–2050.
[45] Yan F, Bai HR, Ge GL, *et al.* Boosting energy storage performance of lead-free ceramics via layered structure optimization strategy. *Small* 2022, **18**: 2202575.
[46] Zeng XF, Lin JF, Dong GL, *et al.* Polymorphic relaxor phase and defect dipole polarization co-reinforced capacitor energy storage in temperature-monitorable high-entropy ferroelectrics. *Nat Commun* 2025, **16**: 1870.
[47] Luangpangai A, Jirattitikarn T, Somsri W, *et al.* Enhanced dielectric and ferroelectric properties near the morphotropic phase boundary in BNBT–BSN ceramics prepared by the solid-state combustion technique. *Sci Rep* 2024, **14**: 30268.
[48] Fu J, Xie AW, Zuo RZ, *et al.* A highly polarizable concentrated dipole glass for ultrahigh energy storage. *Nat Commun* 2024, **15**: 7338.
[49] Kuang HY, He X, Oleg Vy, *et al.* High energy storage and excellent thermal stability in ternary $(1-x)[0.94(Bi_{0.5}Na_{0.5})TiO_3-0.06BaTiO_3]-x Ca(Mg_{1/3}Nb_{2/3})O_3$ lead-free ferroelectric ceramics. *Adv Electron Mater* 2024, **10**: 2300590.
[50] Banerjee K, Asthana S. The effect of A-site cation on ferroelectric properties in $Na_{0.5}Bi_{0.5}TiO_3$-based materials: Correlation between Burns temperature and remanent polarization. *J Appl Phys* 2020, **127**: 144102.
[51] Li F, Zhai JW, Shen B, *et al.* Influence of structural evolution on energy storage properties in $Bi_{0.5}Na_{0.5}TiO_3$–$SrTiO_3$–$NaNbO_3$ lead-free ferroelectric ceramics. *J Appl Phys* 2017, **121**: 054103.
[52] Wu JY, Mahajan A, Riekehr L, *et al.* Perovskite $Sr_x(Bi_{1-x}Na_{0.97-x}Li_{0.03})_{0.5}TiO_3$ ceramics with polar nano regions for high power energy storage. *Nano Energy* 2018, **50**: 723–732.
[53] Li JL, Li F, Xu Z, *et al.* Multilayer lead-free ceramic capacitors with ultrahigh energy density and efficiency. *Adv Mater* 2018, **30**: 1802155.
[54] Xu Q, Liu HX, Zhang L, *et al.* Structure and electrical properties of lead-free $Bi_{0.5}Na_{0.5}TiO_3$-based ceramics for energy-storage applications. *RSC Adv* 2016, **6**: 59280–59291.
[55] Xie AW, Fu J, Zuo RZ, *et al.* Supercritical relaxor nanograined ferroelectrics for ultrahigh-energy-storage capacitors. *Adv Mater* 2022, **34**: 2204356.
[56] Cao WJ, Lin RJ, Hou X, *et al.* Interfacial polarization restriction for ultrahigh energy-storage density in lead-free ceramics. *Adv Funct Mater* 2023, **33**: 2301027.
[57] Kang RR, Wang ZP, Yang WJ, *et al.* Enhanced energy storage performance in $Sr_{0.7}La_{0.2}Zr_{0.15}Ti_{0.85}O_3$-modified $Bi_{0.5}Na_{0.5}TiO_3$ ceramics via constructing local phase coexistence. *Chem Eng J* 2022, **446**: 137105.
[58] Zhou CP, Yan F, Zheng ZH, *et al.* Achieving superior capacitive energy storage in tape-casting fabricated $Bi_{0.5}Na_{0.5}TiO_3$-based relaxor ferroelectrics via multiscale regulation. *Energy Storage Mater* 2025, **75**: 104082.
[59] Li DF, Zheng ZH, Yang B, *et al.* Atomic-scale high-entropy design for superior capacitive energy storage performance in lead-free ceramics. *Adv Mater* 2025, **37**: 2409639.
[60] Dang ST, Peng ZH, Zhang XQ, *et al.* Enhanced energy storage performance of $BiFeO_3$–$BaTiO_3$ based ceramics under moderate electric fields via multiple synergistic design. *Chem Eng J* 2025, **512**: 162494.
[61] Nie XR, Jing RY, Yang YL, *et al.* Synergistic enhancement of energy storage performance in BNT-based ceramics through the co-doping of multiple A-site ions. *Chem Eng J* 2025, **507**: 160500.
[62] Wang CY, Cao WJ, Liang C, *et al.* Equimolar high-entropy for excellent energy storage performance in $Bi_{0.5}Na_{0.5}TiO_3$-based ceramics. *Energy Storage Mater* 2024, **70**: 103534.
[63] Yang YL, Zha JL, Lu XM, *et al.* Excellent energy storage performance of Nd-modified lead-free $AgNbO_3$ ceramics via triple collaborative optimization. *Nano Energy* 2024, **131**: 110242.

[64] Long CB, Su ZQ, Xu AW, *et al.* $Bi_{0.5}Na_{0.5}TiO_3$-based energy storage ceramics with excellent comprehensive performance by constructing dynamic nanoscale domains and high intrinsic breakdown strength. *Nano Energy* 2024, **124**: 109493.

[65] Shi WJ, Zhang LY, Jing RY, *et al.* Moderate fields, maximum potential: Achieving high records with temperature-stable energy storage in lead-free BNT-based ceramics. *Nano-Micro Lett* 2024, **16**: 91.

[66] Tang LM, Yu ZY, Pan ZB, *et al.* Giant energy storage density with antiferroelectric-like properties in BNT-based ceramics via phase structure engineering. *Small* 2023, **19**: 2302346.

[67] Zhao WC, Xu DM, Li D, *et al.* Broad-high operating temperature range and enhanced energy storage performances in lead-free ferroelectrics. *Nat Commun* 2023, **14**: 5725.

[68] Li PX, Wang SM, Qian J, *et al.* Local defect structure design enhanced energy storage performance in lead-free antiferroelectric ceramics. *Chem Eng J* 2024, **497**: 154926.

[69] Shang F, Wei JW, Xu JW, *et al.* Boosting energy storage performance of glass ceramics via modulating defect formation during crystallization. *Adv Sci* 2024, **11**: 2307011.

[70] Lu Y, Wang XC, Li P, *et al.* The grain size and domain structure synergistic effect on BNT based lead-free ceramics with high energy storage properties. *J Energy Storage* 2024, **104**: 114508.

[71] Wang YH, Dang ST, Chai QZ, *et al.* Superior energy storage performance in $Bi_{0.5}Na_{0.5}TiO_3$ based ceramics via synergistic design of multi-size domain construction and multiple phase structures. *Chem Eng J* 2024, **500**: 156460.

[72] Li PZ, Yang HB, Yuan QB, *et al.* Enhanced energy storage performance of $Na_{0.5}Bi_{0.5}TiO_3$-based relaxor ferroelectric ceramics by synergistic optimization strategies. *Mater Today Phys* 2024, **43**: 101420.

[73] Long CB, Zhou WJ, Song HM, *et al.* Simultaneously realizing ultrahigh energy storage density and efficiency in $BaTiO_3$-based dielectric ceramics by creating highly dynamic polar nanoregions and intrinsic conduction. *Acta Mater* 2023, **256**: 119135.